ACS APPLIED MATERIALS & INTERFACES

www.acsami.org

Research Article

Acceleration of DNA Hybridization Chain Reactions on 3D Nanointerfaces of Magnetic Particles and Their Direct Application in the Enzyme-Free Amplified Detection of microRNA

Motoi Oishi* and Shotaro Juji

Cite This: *ACS Appl. Mater. Interfaces* 2021, 13, 35533−35544

Read Online

ACCESS | Metrics & More | Article Recommendations | Supporting Information

ABSTRACT: Accelerated DNA hybridization chain reactions (HCRs) using DNA origami as a scaffold have received considerable attention in dynamic DNA nanotechnology. However, tailor-made designs are essential for DNA origami scaffolds, hampering the practical application of accelerated HCRs. Here, we constructed the semilocalized HCR and localized HCR systems using magnetic beads (MBs) as a simple scaffold to explore them for the enzyme-free miR-21 detection. The semilocalized HCR system relied on free diffusing one hairpin DNA and MBs immobilized with another hairpin DNA, and the localized HCR system relied on MBs coimmobilized with two hairpin DNAs. We demonstrated that the DNA density on MBs plays a critical role in HCR kinetics and limit of detection (LOD). Among semilocalized HCR systems, MBs with a medium DNA density showed a faster HCR and lower LOD (10 pM) than the diffusive (conventional) HCR system (LOD: 86 pM). In contrast, the HCR further accelerated for the localized HCR systems as the DNA density increased. The localized HCR system with the highest DNA density showed the fastest HCR and the lowest LOD (533 fM). These findings are of great importance for the rational design of accelerated HCRs using simple scaffolds for practical applications.

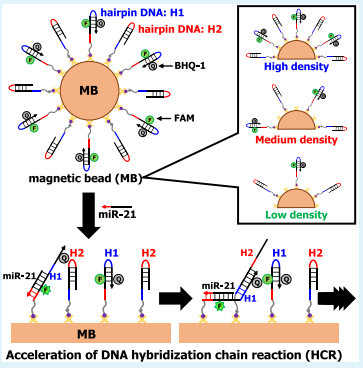

KEYWORDS: *biosensor, DNA hybridization chain reaction, magnetic particle, nanointerface, toehold-mediated DNA displacement reaction*

INTRODUCTION

Dynamic DNA nanotechnology has been used to create nontrivial autonomous functions owing to the programmable, predictable properties and self-assembling of DNA,[1−5] resulting in applications such as biosensors,[6−10] bioimaging,[11−14] nanorobots,[15−20] and computing.[21−24] In particular, cascading toehold-mediated DNA displacement reactions (TMDRs),[1,25−28] such as hybridization chain reactions (HCRs),[29−32] catalytic hairpin assembly reactions (CHAs),[33,34] and entropy-driven catalytic reactions[35] have attracted much attention as enzyme-free driving forces for autonomous function processes in dynamic DNA nanotechnology. However, the rates of the vast majority of HCRs depend on random collisions and interactions between freely diffusing DNA reactants in solution.[36−40] Furthermore, HCRs are typically carried out at low concentrations (nanomolar orders) to avoid leak reactions and undesired TMDRs, which eventually prolong the operation time in the practical applications mentioned above. To overcome this difficulty, a major challenge is to accelerate the rate of HCRs.

A feasible approach in this regard is the use of scaffolds such as DNA origami, DNA nanostructures, and membranes to colocalize DNA reactants in a confined space, thereby maintaining high local concentrations of DNA reactants without increasing the concentration of the total DNA reactants.[41,42] Almost all of the studies reported so far have been limited to the use of DNA-based scaffolds such as long DNA strands[43,44] and DNA origami,[45−47] as they offer precise control of the positioning of DNA reactants on these one- (1D) and two-dimensional (2D) scaffolds, allowing experimental and theoretical analysis of reaction mechanisms and kinetics.[43,45,47] Additionally, localized HCRs on DNA-based scaffolds show accelerated reaction rates and, thus, shorter reaction times compared with diffusive (conventional) HCRs using free DNA reactants. However, successful practical applications of localized HCRs on DNA-based scaffolds have been limited to a few reports[44,46] because localized HCRs are sensitive to defects in these scaffolds, such as non- or miss-immobilized DNA reactants, which can terminate the reactions. In particular, immobilization of DNA reactants on DNA origami scaffolds requires careful positioning. Furthermore, DNA origami scaffolds require costly and time-

Received: May 24, 2021
Accepted: July 11, 2021
Published: July 21, 2021

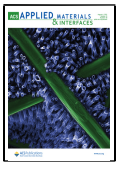

https://doi.org/10.1021/acsami.1c09631
ACS Appl. Mater. Interfaces 2021, 13, 35533−35544

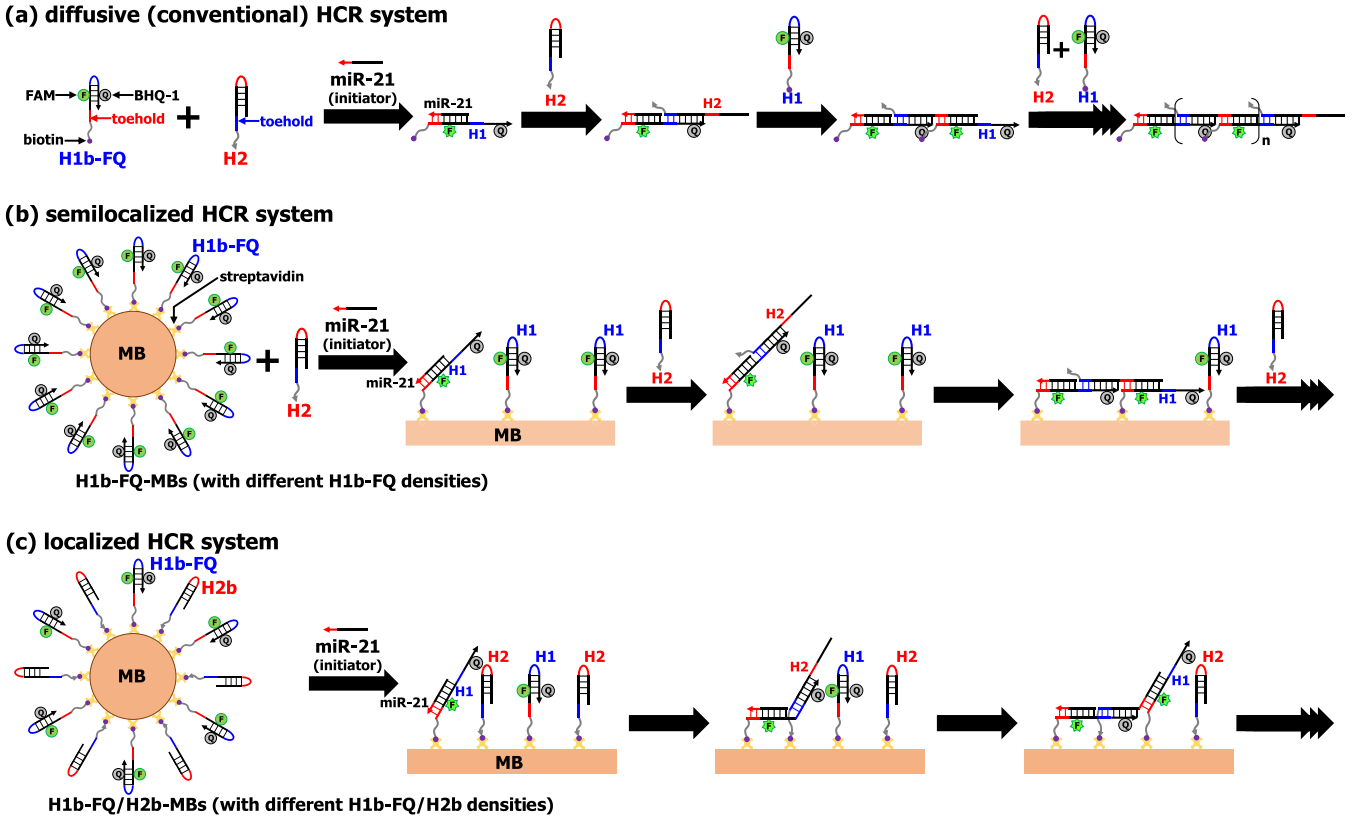

Figure 1. Schematic illustration of the principles of (a) diffusive (conventional) HCR, (b) semilocalized HCR, and (c) localized HCR systems.

consuming preparation of a long circular single-stranded DNA from bacteriophages and tailor-made designs of hundreds of short complementary single-stranded DNAs. Therefore, it is difficult to obtain large quantities of DNA origami scaffolds, which hinders the practical application of the localized HCR. To further integrate localized HCRs into practical applications, it is highly desirable to use simpler three-dimensional (3D) scaffolds that are readily available in large quantities without the need for costly and time-consuming processes or tailor-made designs. However, no systematic studies have been reported on the impact of 3D nanointerface structures of simple scaffolds on HCR kinetics and their performance in practical applications.

Herein, we designed and prepared various DNA-modified magnetic beads (MBs) with different 3D nanointerfaces to make quantitative comparisons of HCR kinetics and explored their potential practical application in biosensors. Commercially available streptavidin-coated MBs have been recognized as a useful and simple 3D scaffold in the field of biosensing[10,48−51] because a wide variety of biotin-modified biomolecules are easily immobilized on the surface of these MBs by washing off nonimmobilized biomolecules under a magnetic field. Figure 1 shows the principle of the diffusive (conventional) HCR system (Figure 1a), semilocalized HCR system (Figure 1b), and localized HCR system (Figure 1c). The semilocalized HCR system was newly constructed using freely diffusing hairpin DNA-2 (H2) and MBs (H1b-FQ-MBs) immobilized with biotin, 6-carboxy fluorescein (FAM), and a black hole quencher-1 (BHQ-1)-labeled hairpin DNA-1 (H1b-FQ) alone, and the localized HCR system was constructed using MBs (H1b-FQ/H2b-MBs) coimmobilized with H1b-FQ and biotin-labeled hairpin DNA-2 (H2b). In addition, MBs with different numbers of immobilized DNAs were used for the semilocalized HCR and localized HCR systems. The self-quenched H1b-FQ was utilized to monitor HCR kinetics in real time through Förster resonance energy transfer (FRET) between FAM and BHQ-1. Homosapiens microRNA-21 (miR-21) was used as an initiator for the HCR and a target miRNA because miR-21 is known to be involved in various diseases; the direct detection of miR-21 from serum and cell lysate is currently one of the major challenges.[52−54] In a semilocalized HCR system (Figure 1b), miR-21 interacts with a toehold of the H1b-FQ on H1b-FQ-MBs and opens the H1b-FQ by TMDR, resulting in the formation of a linear H1b-FQ/miR-21 duplex with a new single-stranded structure. The partial recovery of the fluorescence signal of FAM occurs due to the slight cancelation of FRET by the increased distance between FAM and BHQ-1 from ∼2 to 7 nm since FRET efficiency is known to be dependent on the fluorescence dye-to-quencher separation distance with an inverse sixth power law.[55] Subsequently, a toehold of freely diffusing H2 hybridizes with the single-stranded structure of the H1b-FQ/miR-21 duplex on H1b-FQ-MBs to form the H1b-FQ/miR-21/H2 duplex with a new single-stranded structure. Subsequently, the H1b-FQ/miR-21/H2 duplex searches out unreacted proximate H1b-FQ at the nanointerface of the H1b-FQ-MBs, leading to an HCR between alternating H1b-FQ and H2 on the same H1b-FQ-MB, which results in a semilocalized HCR. Thus, semilocalized HCR initiated by miR-21 affords long-nicked duplexes on the H1b-FQ-MBs. Consequently, the reaction rates and amplification of fluorescence signals are accelerated in the semilocalized HCR system compared to that in the diffusive HCR system because HCRs on MBs proceed only in a confined space where the local concentration of the H1b-FQ

https://doi.org/10.1021/acsami.1c09631
ACS Appl. Mater. Interfaces 2021, 13, 35533−35544

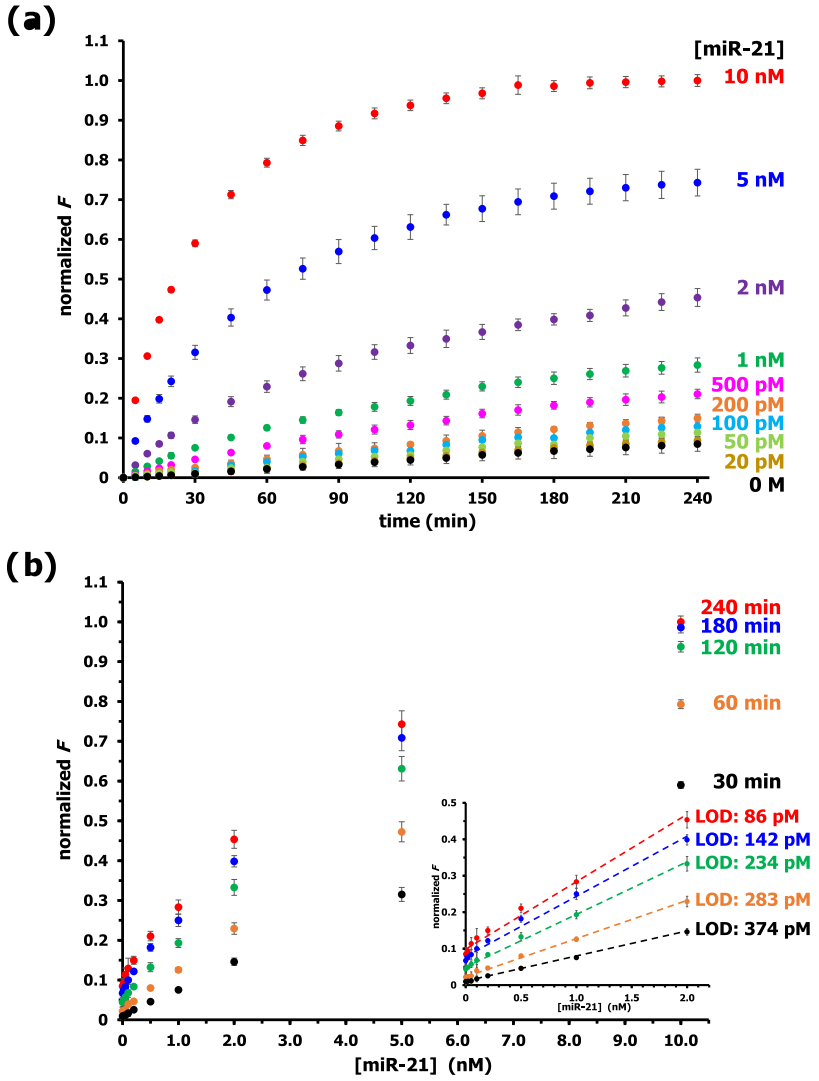

Figure 2. (a) Time-dependent increase in normalized *F* of the diffusive HCR system at different miR-21 concentrations (0−10 nM) in the presence of the H2 (10 nM). (b) Normalized *F* of the diffusive HCR system with various concentrations of miR-21 at different assay times (30 min: black, 60 min: orange, 120 min: green, 180 min: blue, and 240 min: red). The inset shows the responses to 0−2.0 nM miR-21 and LODs at different assay times (30 min: black, 60 min: orange, 120 min: green, 180 min: blue, and 240 min: red). Mean values and standard deviations were obtained from three independent experiments.

increased. Unlike semilocalized HCR systems, localized HCR systems (Figure 1c) rely on the coimmobilization of H1b-FQ and H2b on MBs (H1b-FQ/H2b-MBs), and H1b-FQ and H2b randomly distributed on the surfaces of MBs. Therefore, the H1b-FQ/miR-21 and H1b-FQ/miR-21/H2b duplexes, once formed on the MBs, smoothly hybridize with proximate H2b and proximate H1b-FQ on the MBs, respectively, leading to an HCR only on the same H1b-FQ/H2b-MB (intraparticle HCR), resulting in a fully localized HCR. Eventually, the reaction rates and the amplification of fluorescence signals in localized HCR systems are faster than those in the diffusive HCR and semilocalized HCR systems, because HCR proceeds only in a confined space with increased local concentrations of both H1b-FQ and H2b. In this study, diffusive, semilocalized, and localized HCR systems were applied successfully and directly to enzyme-free miR-21 detection systems using the functions of fluorescence signal amplification, and their HCR kinetics and analytical performance such as the limit of detection (LOD) and assay time were studied comparatively. We demonstrated that the number of immobilized DNAs (i.e., the distance between DNA strands) on MB scaffolds of semilocalized and localized HCR systems played critical roles in their HCR kinetics and analytical performance. The localized HCR system with the largest number of immobilized DNAs showed the most accelerated HCRs and provided the highest sensitivity (LOD: 533 fM in 240 min) and rapid assay time (LOD: 8.9 pM in 30 min) in the miR-21 detection compared to other miR-21-detection systems, including the diffusive HCR system (LOD: 86 pM in 240 min and 374 pM in 30 min) and semilocalized HCR system (LOD: 10 pM in 240 min and 104 pM in 30 min). These findings are of great importance for the rational design of localized HCR systems using simple scaffolds for practical applications.

EXPERIMENTAL SECTION

Preparation of H1b-FQ-MBs (H), (M), and (L). To prepare H1b-FQ-MBs (H), (M), and (L), streptavidin-modified MBs (200 μL, 1.2 × 10^8 particles) were washed using 10 mM Tris−HCl buffer, pH 7.7, containing 150 mM NaCl and 0.01% (v/v) Tween 20 (Tris-buffer) (1000 μL). Since the average number of the immobilized

https://doi.org/10.1021/acsami.1c09631
ACS Appl. Mater. Interfaces 2021, 13, 35533−35544

H1b-FQ strands per MB were controllable by varying the concentrations of added H1b-FQ as shown in Figure S2a, a solution of X nM H1b-FQ in Tris-buffer (1000 μL, X = 500 nM for (H), X = 50 nM for (M), and X = 12.5 nM for (L)) was added to MBs. The resulting suspended mixtures were incubated at 25 °C for 30 min. H1b-FQ-MBs (H), (M), and (L) were washed three times with Tris-buffer (1000 μL) by applying a magnetic field. H1b-FQ-MBs (H), (M), and (L) were dispersed in the same buffer to adjust 100 nM of H1b-FQ. To quantify the amount of immobilized H1b-FQ strands on MBs, FAM- and biotin-labeled H1 (H1b-F) was used in place of H1b-FQ, and the quantitation was carried out according to our previous report.[10]

Preparation of H1b-FQ/H2b-MBs (H), (M), and (L). To prepare H1b-FQ/H2b-MBs (H), (M), and (L), streptavidin-modified MBs (200 μL, 1.2 × 10^8 particles) were washed using Tris-buffer (1000 μL). Since the average numbers of the immobilized H1b-FQ and H2b strands per MB were controllable by varying the concentrations of added H1b-FQ and H2b as shown in Figure S6a, both solutions of X nM H1b-FQ and X nM H2b in Tris-buffer (500 μL each, X = 500 nM for (H), X = 50 nM for (M), and X = 12.5 nM for (L)) were added to MBs. The resulting suspended mixtures were incubated at 25 °C for 30 min. H1b-FQ/H2b-MBs (H), (M), and (L) were washed three times with Tris-buffer (1000 μL) by applying a magnetic field. H1b-FQ/H2b-MBs (H), (M), and (L) were dispersed in the same buffer to adjust 100 nM of H1b-FQ. To quantify the amount of immobilized H1b-FQ and H2b strands on MBs, H1b-F and Alexa 647- and biotin-labeled H2 (H2b-A) were used in place of H1b-FQ and H2b, respectively, and the quantitation was carried out according to our previous report.[10]

Detection of miR-21 by Diffusive HCR, Semilocalized HCR, or Localized HCR Systems. For the diffusive HCR system, 400 nM H1b-FQ and 400 nM H2 in Tris-buffer were separately annealed at 90 °C for 1 min before use. To the mixture of Tris-buffer and 10 mM Tris−HCl buffer, pH 7.7, containing 150 mM NaCl, 0.01% (v/v) Tween 20, and 250 mM of $MgCl_2$ (Tris-buffer with Mg) (10 μL), both solutions of 400 nM H1b-FQ and 400 nM H2 in Tris-buffer (5 μL each) were added. After that, various concentrations of miR-21 (5 μL, 800 pM to 400 nM) dissolved in Tris-buffer were added to the mixture, and the total volume was 200 μL. Final concentrations of Mg^{2+}, H1b-FQ, H2, and miR-21 were 12.5 mM, 10 nM, 10 nM, and 0−10 nM, respectively. The reaction mixtures were incubated at 25 °C for 240 min, and their fluorescence intensities at 522 nm were measured at appropriate time intervals during incubation.

For the semilocalized HCR system, 100 nM H1b-FQ-MBs (H), (M), and (L) and 400 nM H2 in Tris-buffer were separately annealed at 90 °C for 1 min before use. The MBs are known to scatter excitation light and fluorescence signals only when they are present in high concentrations, affecting the fluorescence signals. Therefore, we performed the experiments in the concentration range of MBs that does not affect the fluorescence signals. As an example, the detection procedure using the H1b-FQ-MB (M) is described as follows: A solution of 100 nM H1b-FQ-MB (M) in Tris-buffer (20 μL, [H1b-FQ] = 100 nM) was added to a 0.5 mL PCR tube, and the buffer solution was removed from the tube by applying a magnetic field. To the H1b-FQ-MB (M), Tris-buffer (180 μL), Tris-buffer with Mg (10 μL), 400 nM H2 in Tris-buffer (5 μL), and various concentrations of miR-21 (5 μL, 200 pM to 400 nM) dissolved in Tris-buffer were added. The total volume and final concentrations of Mg^{2+}, DNAs, and miR-21 were the same as described above. The fluorescence intensity at 522 nm as a function of time was measured in the same way as described above.

For the localized HCR system, each 100 nM H1b-FQ/H2b-MBs (H), (M), and (L) in Tris-buffer was annealed at 90 °C for 1 min before use. As an example, the detection procedure using the H1b-FQ/H2b-MB (H) is described as follows. A solution of 100 nM H1b-FQ/H2b-MB (H) in Tris-buffer (20 μL, [H1b-FQ] = 100 nM and [H2b] = 95 nM) was added to a 0.5 mL PCR tube, and the buffer solution was removed from the tube by applying a magnetic field. To H1b-FQ/H2b-MB (H), Tris-buffer (175 μL), Tris-buffer with Mg (10 μL), and various concentrations of miR-21 (5 μL, 8 pM to 400 nM) dissolved in Tris-buffer were added. The total volume and final concentrations of Mg^{2+}, DNAs, and miR-21 were the same as described above. The fluorescence intensity at 522 nm as a function of time was measured in the same way as described above.

RESULTS AND DISCUSSION

Diffusive HCR System. The DNA and RNA sequences are shown in Table S1. To verify the feasibility of the HCR with H1b-FQ, H2, and miR-21, a diffusive HCR system (Figure 1a) was initially carried out in 10 mM Tris−HCl buffer at pH 7.7, containing 150 mM NaCl, 12.5 mM $MgCl_2$, and 0.01% (v/v) Tween 20 at 25 °C for 240 min, with H1b-FQ (10 nM), H2 (10 nM), and different concentrations of miR-21 (0−10 nM). The change in the normalized fluorescence intensities (F) as a function of time is shown in Figure 2a, and the normalized F was defined as follows: Normalized $F = (F_t - F_0)/(F_{max} - F_0)$, where F_t, F_0, and F_{max} are the fluorescence intensities at t min, at 0 min, and of the H1b-FQ/miR-21/H2 duplex (10 nM) prepared by annealing process of the H1b-FQ, miR-21, and H2, respectively. Thus, when the normalized F is 1.0, it corresponds to the fact that H1b-FQ has completely reacted. Notably, the increase in both the values and rates of the normalized F was significantly observed with increasing amounts of miR-21, indicating the occurrence of HCR triggered by miR-21. However, the normalized F slightly increased even in the absence of miR-21 (0 M) due to leakage caused by undesired hybridization between H1b-FQ and H2.[29−32] Additional evidence for the HCR of H1b and H2 triggered by miR-21 was obtained by 2.0% agarose gel electrophoresis (Figure S1). In the mixture of H1b and H2 in the absence of miR-21 (Figure S1, lane 5), any bands at higher molecular weight regions did not appear; thus, only a single band was observed. Additionally, the migration position of the band was the same as those of the bands for H1b alone and H2 alone (Figure S1, lanes 3 and 4), demonstrating that hybridization of H1b and H2 is negligible under these experimental conditions. Notably, the molecular weight of the smear bands corresponding to the HCR products increased with a decrease in the amount of miR-21 (Figure S1, lanes 6 (1.0 × miR-21), 7 (0.1 × miR-21), and 8 (0.01 × miR-21)), whereas unreacted H1b and H2 were clearly observed for the HCR sample using the smallest amount of miR-21 (Figure S1, lane 8). Taken together, these facts demonstrate that HCR occurs in a manner dependent on the amount of miR-21, suggesting the potential for quantitative detection of miR-21. Additionally, linear relationships were observed between normalized F and low concentrations of miR-21 (<2 nM) for each assay time (30, 60, 120, 180, and 240 min) (Figure 2b). The LOD was calculated as the mean ± 3σ, where mean and σ are the normalized F in the absence of miR-21 (0 M) and its standard deviation, respectively. The LODs decreased with increasing assay time, reaching the lowest LOD (86 pM) after 240 min, and these LODs were comparable to other reported diffusive (conventional) HCRs.[56]

Semilocalized HCR System. To substantiate the effect of nanointerface structures of MB scaffolds (diameter: 3 μm) on semilocalized HCRs, we designed and prepared three types of H1b-FQ-MBs with different numbers of immobilized H1b-FQ strands, namely, high density (H), medium density (M), and low density (L). The average number of immobilized H1b-FQ strands per MB scaffold, the average distance between the H1b-FQ strands, and the calculated local concentration of the H1b-FQ strands are shown in Figures 3a and S2. Figure 3b−d

https://doi.org/10.1021/acsami.1c09631
ACS Appl. Mater. Interfaces 2021, 13, 35533−35544

(a)

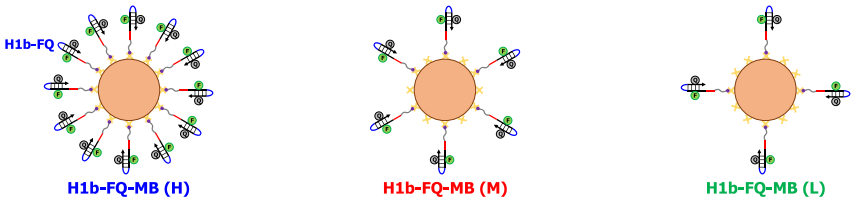

	H1b-FQ-MB (H)	H1b-FQ-MB (M)	H1b-FQ-MB (L)
number of the H1b-FQ (strands/MB)	$(7.5 \pm 0.3) \times 10^5$	$(2.4 \pm 0.2) \times 10^5$	$(5.3 \pm 0.2) \times 10^4$
distance between the H1b-FQ strands (nm)	7.0 ± 0.2	12.3 ± 0.1	26.2 ± 0.5
local concentration of the H1b-FQ (mM)	23.8 ± 1.1	7.6 ± 0.1	1.7 ± 0.1

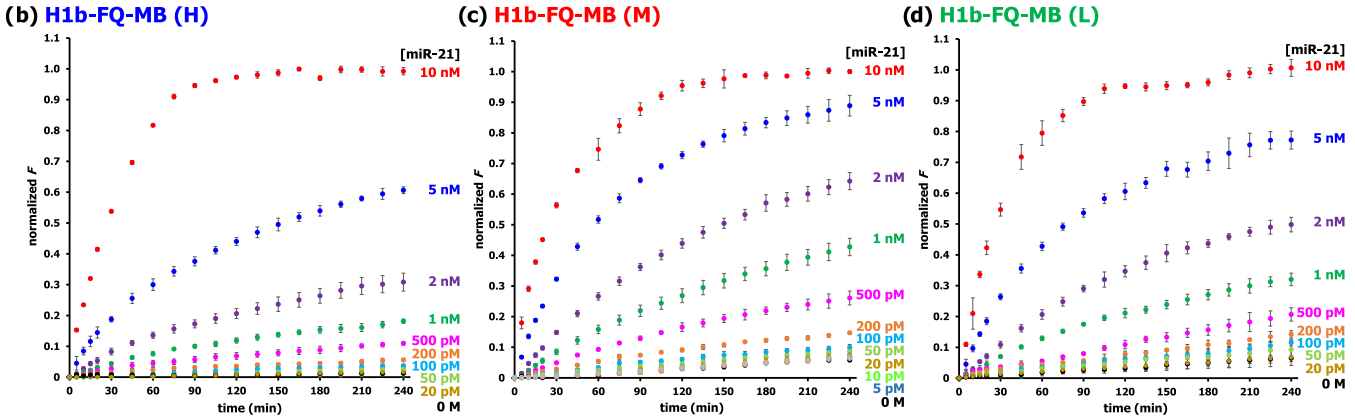

Figure 3. (a) Average number of the immobilized H1b-FQ strands per MB scaffold, average distance between the H1b-FQ strands on the MB, and the calculated local concentration of H1b-FQ for H1b-FQ-MBs (H), (M), and (L). Time-dependent increase in normalized F of the (b) H1b-FQ-MB (H), (c) H1b-FQ-MB (M), and (d) H1b-FQ-MB (L) at different miR-21 concentrations (0−10 nM) in the presence of the H2 (10 nM). Mean values and standard deviations were obtained from three independent experiments.

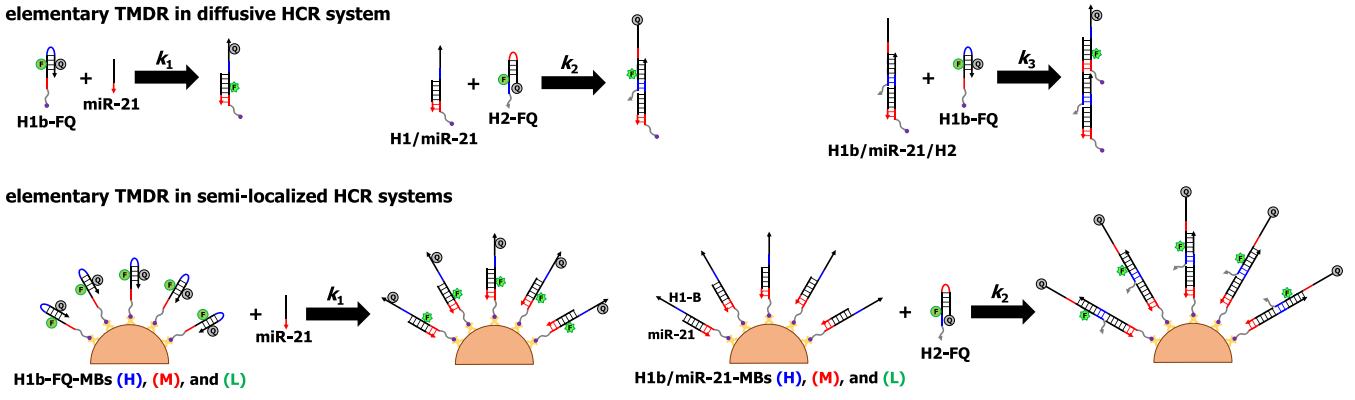

	k_1 (M^{-1} s^{-1})	k_2 (M^{-1} s^{-1})	k_3 (M^{-1} s^{-1})
diffusive HCR system	$(4.2 \pm 0.1) \times 10^5$	$(6.8 \pm 0.7) \times 10^4$	$(7.2 \pm 0.6) \times 10^4$
semi-localized HCT systems			
H1b-FQ-MB (H) for k_1 and H1b/miR-21-MB (H) for k_2	$(2.9 \pm 0.2) \times 10^5$	$(1.5 \pm 0.2) \times 10^4$	—
H1b-FQ-MB (M) for k_1 and H1b/miR-21-MB (M) for k_2	$(3.8 \pm 0.4) \times 10^5$	$(5.3 \pm 0.3) \times 10^4$	—
H1bFQ-MB (L) for k_1 and H1b/miR-21-MB (L) for k_2	$(3.8 \pm 0.5) \times 10^5$	$(5.0 \pm 0.4) \times 10^4$	—

Figure 4. Each elementary TMDR in both the diffusive and the semilocalized HCR systems (H1b-FQ-MBs (H), (M), and (L)) and their reaction rate constants (k_1, k_2, and k_3). The k_3 of the semilocalized HCR systems is excluded. Mean values and standard deviations were obtained from three independent experiments.

shows the time-dependent increase in the normalized F for H1b-FQ-MBs (H), (M), and (L) (all [H1b-FQ] = 10 nM) in the presence of H2 (10 nM) at different concentrations of miR-21 (0−10 nM). Similar to the diffusive HCR system (Figure 2a), the normalized F for all semilocalized HCR systems increased, where the increase in both the values and rates of the normalized F was significantly observed with increasing amount of miR-21. Although the normalized F for H1b-FQ-MBs (M) and (L) slightly increased even in the absence of miR-21 (0 M) (leakage), H1b-FQ-MBs (H) showed only negligible leakage (normalized F < 0.02). To compare the kinetics of diffusive and semilocalized HCR systems, the time needed to reach the normalized F value of 0.1 (normalized F = 0.1) triggered by 1.0 nM miR-21 was defined as the C_t value. The C_t values for the diffusive HCR system and H1b-FQ-MBs (H), (M), and (L) were estimated to be 45, 90, 35, and 45 min, respectively. Notably, the HCR kinetics of H1b-FQ-MBs (M) (C_t = 35 min) was faster than

https://doi.org/10.1021/acsami.1c09631
ACS Appl. Mater. Interfaces 2021, 13, 35533−35544

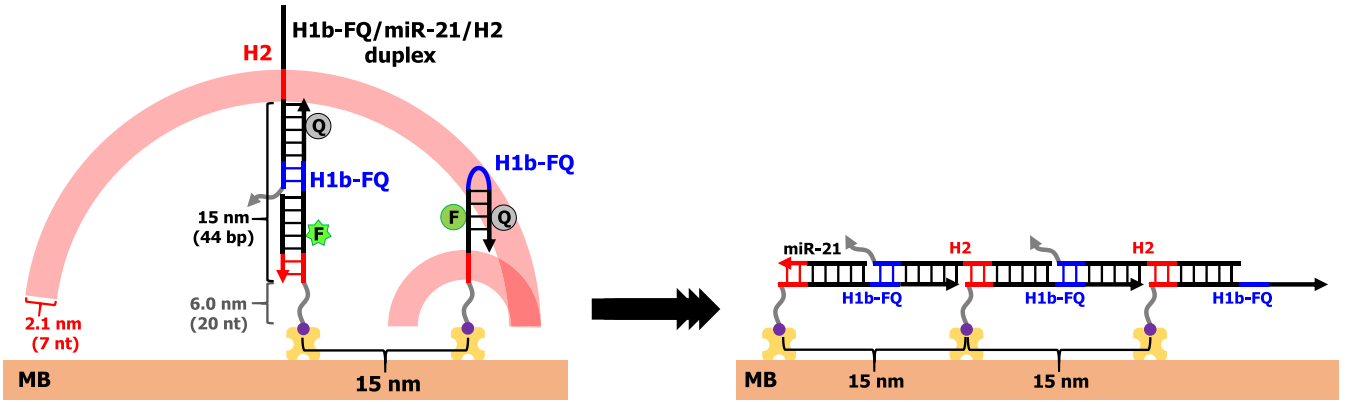

Figure 5. Geometric illustration of the critical distance between the miR-21/H1b-FQ/H2 duplex and the unreacted H1b-FQ on the nanointerface of MBs (using 0.34 nm/bp for dsDNA and 0.30 nm/nt for ssDNA). The critical distance for the semilocalized HCR system was calculated as follows: critical distance (nm) = (44 bp: 15 nm + 20 nt: 6 nm in H1b-FQ/miR-21/H2 duplex) − (20 nt: 6 nm in H1b-FQ).

that of the diffusive HCR system (C_t = 45 min, [H1b-FQ] = 10 nM) because of the occurrence of semilocalized HCRs by the proximate effect with a significant increase in the local concentrations of H1b-FQs (local [H1b-FQ] = 7.6 mM). In sharp contrast, H1b-FQ-MBs (H) (C_t = 90 min) showed the slowest HCR kinetics despite having the largest number of immobilized H1b-FQ strands and, thus, the highest local concentration of H1b-FQ (local [H1b-FQ] = 23.8 mM). Additionally, although the H1b-FQ-MBs (L) (local [H1b-FQ] = 1.7 mM) had a higher local concentration of H1b-FQ than the diffusive HCR system, the HCR kinetics of H1b-FQ-MBs (L) (C_t = 45 min) were comparable to those of the diffusive HCR system (C_t = 45 min).

To further clarify the effect of the number of immobilized H1b-FQ strands on the kinetics of semilocalized HCRs, we first focused on three elementary reactions of semilocalized HCR (polymerization), which included the TMDR of H1b-FQ with miR-21 (initiation), TMDR of the H1b-FQ/miR-21 duplex with freely diffusing H2 (propagation), and localized TMDR of the H1b-FQ/miR-21/H2 duplex with the proximate H1b-FQ on MBs (propagation). TMDRs have been well studied, and their kinetics are usually applicable to a bimolecular kinetic model without back reactions when an appropriate toehold length exists (see the kinetic model for TMDRs, Supporting Information).[25−28] Figure 4 shows each elementary TMDR in both diffusive and semilocalized HCR systems and their reaction rate constants (k_1: initiation, k_2: propagation, and k_3: propagation), except for the k_3 of the localized TMDR of the H1b-FQ/miR-21/H2 with the proximate H1b-FQ on MBs. The reason for excluding the localized TMDR of the H1b-FQ/miR-21/H2 with the proximate H1b-FQ is that the reaction is expected to be very fast, and it is difficult to prepare a suitable reaction system and determine the rate constant (k_3) experimentally. To determine the individual reaction rate constants k_1 and k_2, each TMDR was carried out under the same reaction conditions as above, with the concentrations of all DNA at 10 nM. The change in the normalized F as function of time was monitored (Figure S3), and the reaction rate constants were determined from the bimolecular kinetic equation (see eq SI(4), Supporting Information). In all cases, the reaction rate constants k_2 were ∼1 order of magnitude smaller than the reaction rate constants k_1, indicating that the propagation step of TMDRs of H1b-FQ/miR-21 with the freely diffusing H2 is the rate-determining step in HCRs. Notably, although the reaction rate constant k_1 for H1b-FQ-MB (H) with the largest number of immobilized H1b-FQ strands is comparable to those of other H1b-FQ-MBs (M) and (L), the reaction rate constant k_2 for H1b/miR-21-MB (H) is ∼4.5 and 3.5 times lesser than those for the diffusive HCR system and other H1b/miR-21-MBs (M) and (L), respectively. This is most likely the strong electrostatic repulsion between the dense H1b/miR-21 duplexes on H1b/miR-21-MBs (H) and the freely diffusing H2-FQs, resulting in the slowest HCR in H1b-FQ-MBs (H) (C_t = 90 min) as well as negligible leakage (normalized F <0.02). It has been reported that TMDRs at the particle−liquid interface (pseudo-heterogeneous reactions) are greatly affected by the number of immobilized DNAs (i.e., charge density).[20,57−60] In contrast, the reaction rate constants k_2 for H1b/miR-21-MBs (M) and (L), with a smaller number of immobilized H1b/miR-21 duplexes compared with H1b/miR-21-MB (H), were at the same level as that of the diffusive HCR system due to reduced electrostatic repulsion between the H1b/miR-21 duplexes on the MBs and the freely diffusing H2-FQs. Although the reaction rate constants k_1 and k_2 for the H1b-FQ-MBs (M) and (L) were almost the same, an accelerated HCR was observed only for H1b-FQ-MB (M) (C_t = 35 min), but not for H1b-FQ-MB (L) (C_t = 45 min), indicating that this acceleration is based on the proximate effect with a significant increase in the local concentration of H1b-FQs (7.6 mM) on MBs.

To understand the acceleration of HCR observed only in H1b-FQ-MBs (M), it should be ascertained whether HCRs occur on the nanointerface of the H1b-FQ-MB (intraparticle HCR: semilocalized HCR) or between the H1b-FQ-MBs (interparticle HCR), because the H1b-FQ/miR-21/H2 duplex formed on the H1b-FQ-MBs with a small number of immobilized H1b-FQ strands (low density of H1b-FQ: long distance between H1b-FQ strands) easily interacts with any other freely diffusing H1b-FQ-MBs (interparticle HCR). In this regard, the time-dependent changes in the sizes of the H1b-FQ-MBs (H), (M), and (L) in the presence of H2 (10 nM) and miR-21 (1.0 nM) were monitored by dynamic light scattering (DLS) measurements (Figure S4). If HCRs only occurred on nanointerfaces on the same MBs (intraparticle HCR: semilocalized HCR), no change in the size of MBs would be observed as a function of time. Additionally, the sizes of MBs should increase as a function of time for the HCRs occurring between the freely diffusing MBs (interparticle HCR). In fact, changes in the sizes of H1b-FQ-MB (H) and

https://doi.org/10.1021/acsami.1c09631
ACS Appl. Mater. Interfaces 2021, 13, 35533−35544

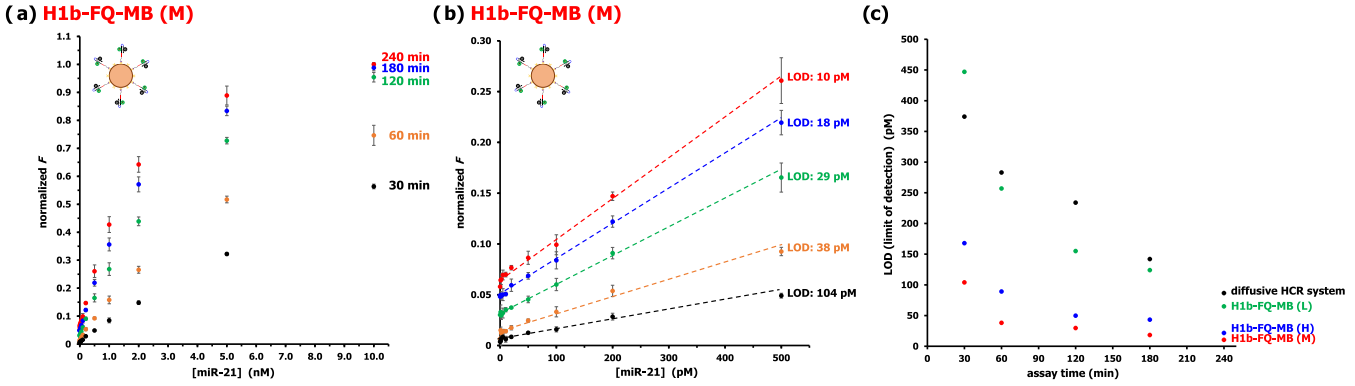

Figure 6. (a) Normalized *F* of the H1b-FQ-MB (M) with various concentrations of miR-21 at different assay times (30 min: black, 60 min: orange, 120 min: green, 180 min: blue, and 240 min: red). (b) Normalized *F* and LODs of the H1b-FQ-MB (M) responses to 0−500 pM of miR-21 at different assay times (30 min: black, 60 min: orange, 120 min: green, 180 min: blue, and 240 min: red). Mean values and standard deviations were obtained from three independent experiments. (c) LODs of the diffusive HCR system and the semilocalized HCR systems using H1b-FQ-MBs (H), (M), and (L) at different assay times (30, 60, 120, 180, and 240 min).

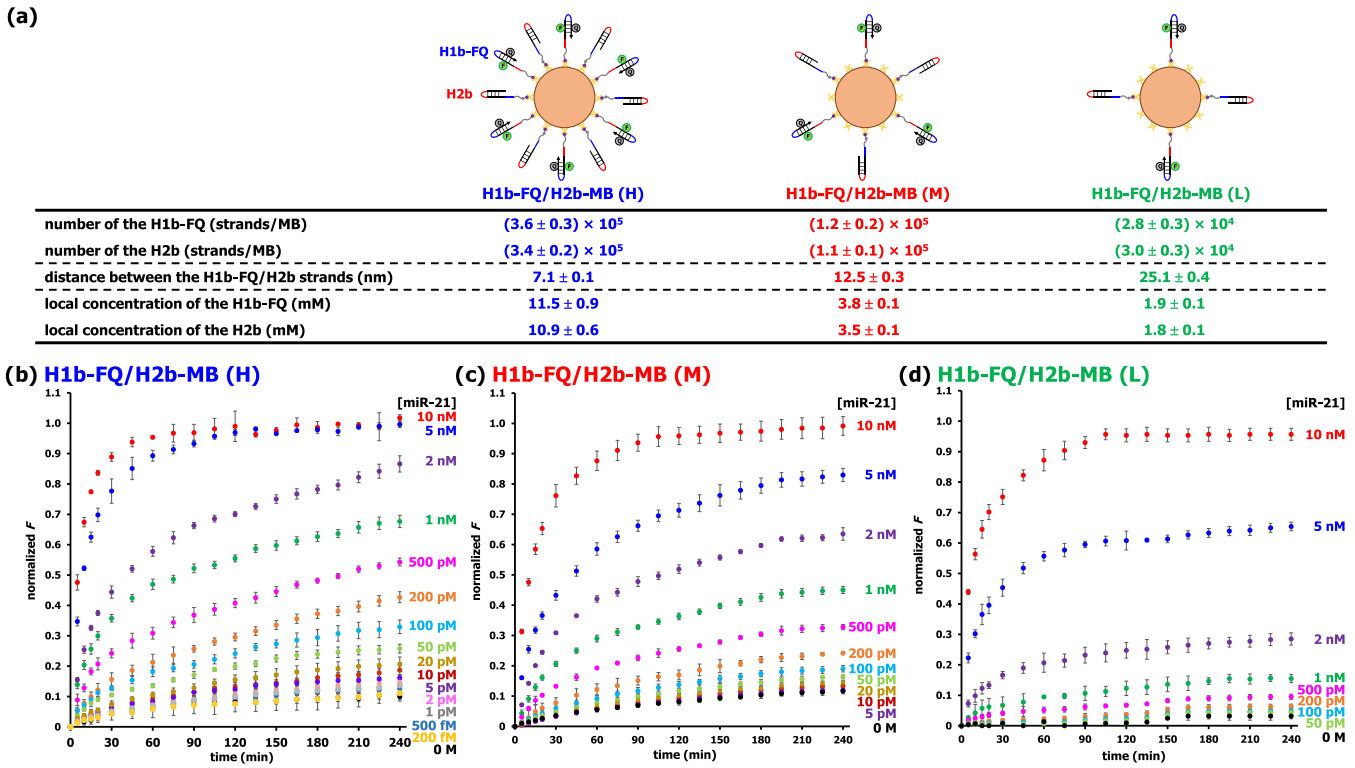

	H1b-FQ/H2b-MB (H)	H1b-FQ/H2b-MB (M)	H1b-FQ/H2b-MB (L)
number of the H1b-FQ (strands/MB)	$(3.6 \pm 0.3) \times 10^5$	$(1.2 \pm 0.2) \times 10^5$	$(2.8 \pm 0.3) \times 10^4$
number of the H2b (strands/MB)	$(3.4 \pm 0.2) \times 10^5$	$(1.1 \pm 0.1) \times 10^5$	$(3.0 \pm 0.3) \times 10^4$
distance between the H1b-FQ/H2b strands (nm)	7.1 ± 0.1	12.5 ± 0.3	25.1 ± 0.4
local concentration of the H1b-FQ (mM)	11.5 ± 0.9	3.8 ± 0.1	1.9 ± 0.1
local concentration of the H2b (mM)	10.9 ± 0.6	3.5 ± 0.1	1.8 ± 0.1

Figure 7. (a) Average number of the immobilized H1b-FQ and H2b strands per MB scaffold, average distance between the H1b-FQ/H2b strands on the MB, and calculated local concentrations of H1b-FQ and H2b for H1b-FQ/H2b-MBs (H), (M), and (L). Time-dependent increase in the normalized *F* of the (b) H1b-FQ/H2b-MB (H), (c) H1b-FQ/H2b-MB (M), and (d) H1b-FQ/H2b-MB (L) at different miR-21 concentrations (0−10 nM). Mean values and standard deviations were obtained from three independent experiments.

the H1b-FQ-MB (M) were not observed for 240 min (Figure S4a,b), strongly indicating that the HCRs (intraparticle HCR: semilocalized HCR) occurred on nanointerfaces of the same H1b-FQ-MB (H) and H1b-FQ-MB (M). In sharp contrast, the sizes of H1b-FQ-MBs (L) with the smallest number of immobilized H1b-FQ strands gradually increased as a function of time, which finally caused the aggregation of H1b-FQ-MBs (L) at 240 min (Figure S4c), clearly indicating that an interparticle HCR had occurred. It seems to be the shorter average distance between the H1b-FQ strands on the H1b-FQ-MB (H) (7.0 nm) and the H1b-FQ-MB (M) (12.3 nm) facilitates intraparticle HCRs (semilocalized HCRs) smoothly through the proximate effect with a significant increase in local concentrations of H1b-FQ on MBs, but the proximate effect is limited for H1b-FQ-MBs (L), where there is a longer average distance between the H1b-FQ strands (26.2 nm).

To consider the effect of the average distance between the H1b-FQ strands on HCR kinetics, Figure 5 shows a geometric illustration of the critical distance between the H1b-FQ/miR-21/H2 duplex and the unreacted H1b-FQ on the nanointerface of MBs when the lengths of single-stranded DNA (ssDNA) and double-stranded DNA (dsDNA) are 3.0 nm per 10 nucleotides (nts) and 3.4 nm per 10 base pairs (bp),[61] respectively. TMDR involves a two-step process; the formation

https://doi.org/10.1021/acsami.1c09631
ACS Appl. Mater. Interfaces 2021, 13, 35533−35544

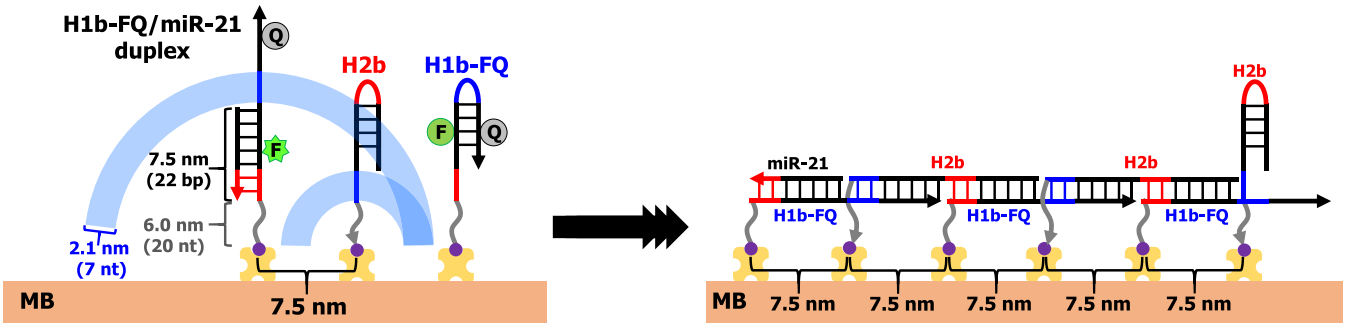

Figure 8. Geometric illustration of the critical distance between the H1b-FQ/miR-21 duplex and the unreacted H2b on the nanointerface of MBs (using 0.34 nm/bp for dsDNA and 0.6 nm/nt for ssDNA). The critical distance for the semilocalized HCR system was calculated as follows: critical distance (nm) = (22 bp: 7.5 nm + 20 nt: 6 nm in H1b-FQ/miR-21 duplex) − (20 nt: 6 nm in H2b).

of several base pairs at the toehold domains and the branch migration process, and the former process is known to be the rate-determining step.[25] Therefore, the most important factor for the TMDR in HCRs on MBs is whether the toehold domain (red color in Figure 5) of the unreacted H1b-FQ and the complementary single-stranded domain (red color in Figure 5) exposed from the H1b-FQ/miR-21/H2 duplex are located at a distance where they can successively interact with each other. We calculated that the critical distance at which the toehold of the unreacted H1b-FQ and the complementary single-stranded domain exposed from the H1b-FQ/miR-21/H2 duplex could interact was ∼15 nm. Therefore, the interparticle HCR was observed only for H1b-FQ-MBs (L) with a longer average distance between the H1b-FQ strands (26.2 nm) compared with the critical distance (15 nm).These facts indicate that the number of immobilized H1b-FQ strands (i.e., average distance between the H1b-FQ strands) on the MBs is a critical factor for intraparticle HCRs (semilocalized HCRs) at the nanointerfaces.

Figures 6a and S5 show the normalized *F* of the H1b-FQ-MB (M) and the other two H1b-FQ-MBs (H) and (L) with various concentrations of miR-21 at different assay times (30, 60, 120, 180, and 240 min), respectively. The linear relationships were observed between the normalized *F* and low concentrations of miR-21 for each assay time, e.g., the linear dynamic range of H1b-FQ-MBs (M) was from 5.0 pM to 2.0 nM. The LODs of all H1b-FQ-MBs (H), (M), and (L) decreased with an increase in the assay time, reaching the lowest LODs after 240 min (Figures 6b and S5). Taking the H1b-FQ-MBs (M) as an example, the LODs were 104, 38, 29, 18, and 10 pM at 30, 60, 120, 180, and 240 min, respectively (Figure 6b). It should be noted that H1b-FQ-MBs (M) achieved the lowest LODs (10 pM at 240 min) compared to H1b-FQ-MBs (H) (LOD: 21 pM at 240 min) and (L) (LOD: 65 pM at 240 min) because the HCR was most accelerated on MBs through the intraparticle semilocalized HCR mechanism (Figure 6c). Furthermore, although H1b-FQ-MBs (H) (C_t = 90 min) showed a slower HCR than the diffusive HCR system (C_t = 45 min), the H1b-FQ-MB (H) (LOD: 21 pM at 240 min) also had significantly lower LODs than the diffusive HCR system (LOD: 86 pM at 240 min). It is possible that the slowest TMDRs on the H1b-FQ-MB (H) caused not only the slowest HCR but also prevented leakage as much as possible, allowing a higher signal-to-noise ratio than the diffusive HCR system. On the other hand, as expected, LODs of H1b-FQ-MB (L) were similar to those of the diffusive HCR system because interparticle HCR was observed only for H1b-FQ-MBs (L).

Localized HCR System. We designed and prepared localized HCR systems including H1b-FQ/H2b-MBs (H), (M), and (L) with different total numbers of immobilized H1b-FQ and H2b strands for comparison with the diffusive and semilocalized HCR systems immobilized with H1b-FQ strands alone. The average number of H1b-FQ and H2b strands per MB scaffold, average distance between H1b-FQ and H2b strands, and the calculated total local concentrations of H1b-FQ and H2b strands are shown in Figures 7a and S6. Figure 7b−d shows the normalized *F* for H1b-FQ/H2b-MBs (H), (M), and (L) (all [H1b-FQ] = 10 nM) at different concentrations of miR-21 (0−10 nM) as a function of time. Similar to the diffusive HCR system (Figure 2a) and semilocalized HCR systems (Figure 3b−d), the normalized *F* for H1b-FQ/H2b-MBs (H), (M), and (L) also increased, and the increase in both the values and rates of the normalized *F* was significantly observed with increasing the amount of miR-21. Although a slight increase in the normalized *F* (leakage) was observed for H1b-FQ/H2b-MBs (H) and (M) even in the absence of miR-21 (0 nM), the H1b-FQ/H2b-MB (L) showed only negligible leakage (normalized *F* <0.04). The C_t values for H1b-FQ/H2b-MBs (H), (M), and (L) were estimated to be 3.6, 12, and 87 min, respectively, viz., the H1b-FQ/H2b-MB (H), with the largest number of immobilized H1b-FQ and H2b strands, showed the fastest HCR kinetics. Notably, the HCR kinetics of H1b-FQ/H2b-MBs (H) was faster than those of the semilocalized HCR system of H1b-FQ-MBs (M), which showed the fastest HCR kinetics among the semilocalized HCR systems. In fact, ∼12.5 and 10 times the acceleration of HCRs were observed for H1b-FQ/H2b-MBs (H) (C_t = 3.6 min) compared to the diffusive HCR system (C_t = 45 min) and H1b-FQ-MBs (M) (C_t = 35 min), respectively. The significant acceleration of HCRs observed for H1b-FQ/H2b-MBs (H) is due to the absence of the rate-determining step in the HCR, that is the TMDR with freely diffusing H2 (k_2), as seen in the semilocalized HCR systems. Thus, the localized HCR on H1b-FQ/H2b-MBs (H) occurred by a proximate effect with a significant increase in the local concentrations of H2b (10.9 mM) and H1b-FQ (11.5 mM), unlike the semilocalized HCR system of H1b-FQ-MBs (M) (local [H1b-FQ] = 7.6 mM, [H2] = 10 nM). The acceleration of the HCR in H1b-FQ/H2b-MBs (M) was also observed, that is the HCR kinetics of H1b-FQ/H2b-MB (M) (C_t = 12 min) was ∼3 times faster than that of H1b-FQ-MB (M) (C_t = 35 min). In sharp contrast, the HCR kinetics of H1b-FQ/H2b-MB (L) (C_t = 87 min) was slower than that of the diffusive HCR system (C_t = 45 min), and the HCR kinetics of H1b-

https://doi.org/10.1021/acsami.1c09631
ACS Appl. Mater. Interfaces 2021, 13, 35533−35544

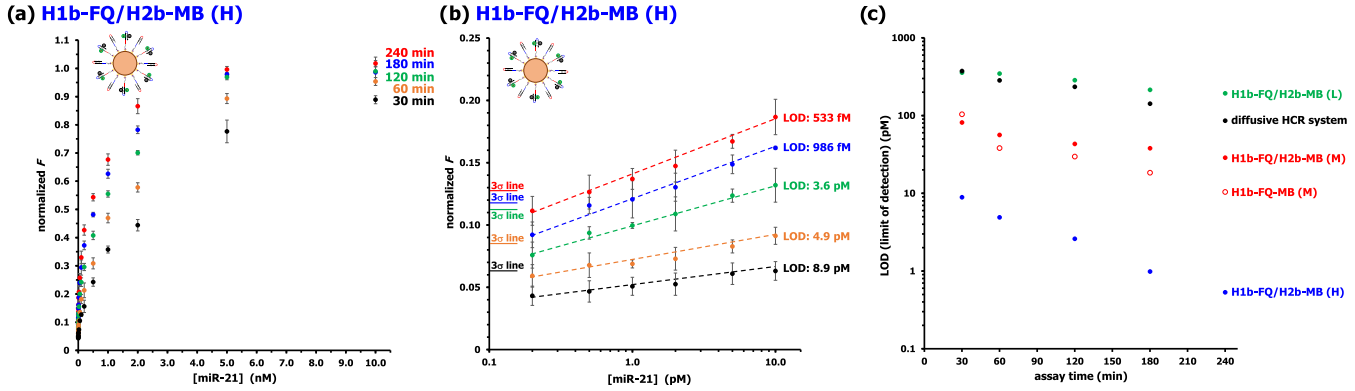

Figure 9. (a) Normalized *F* of the H1b-FQ/H2b-MB (H) with various concentrations of miR-21 at different assay times (30 min: black, 60 min: orange, 120 min: green, 180 min: blue, and 240 min: red). (b) Normalized *F* and LODs of the H1b-FQ/H2b-MB (H) responses to 0−10 pM of miR-21 at different assay times (30 min: black, 60 min: orange, 120 min: green, 180 min: blue, and 240 min: red). Mean values and standard deviations were obtained from three independent experiments. (c) LODs of the diffusive HCR system, the semilocalized system (the H1b-FQ-MB (M)), and the localized HCR systems using H1b-FQ/H2b-MBs (H), (M), and (L) at different assay times (30, 60, 120, 180, and 240 min).

FQ/H2b-MB (L) were comparable to that of H1b-FQ-MB (H) (C_t = 90 min). Unlike all other HCR systems, only the H1b-FQ/H2b-MB (L) slightly increased the normalized *F* as a function of time.

Figure 8 shows a geometric illustration of the critical distance between the H1b-FQ/miR-21 duplex and the unreacted H2b on the nanointerface of MBs to understand the difference in HCR kinetics between H1b-FQ/H2b-MBs (H), (M), and (L). The critical distance at which the toehold (blue color in Figure 8) of the unreacted H2b and the complementary single-stranded domain (blue color in Figure 8) exposed from the H1b-FQ/miR-21 duplex could interact was calculated to be ∼7.5 nm. Therefore, the H1b-FQ/H2b-MB (H), with a shorter average distance (7.1 nm) compared with the critical distance (7.5 nm), facilitated the localized HCR, whereas H1b-FQ/H2b-MBs (M) (12.5 nm) and (L) (25.1 nm), with a longer average distance, were less likely to cause localized HCRs. In particular, the H1b-FQ/H2b-MB (L), with the longest average distance (25.1 nm), no longer caused the HCR by termination at the step of the formation of the H1b-FQ/miR-21 duplex (initiation step) on the MB, resulting in a slight time-dependent increase in the normalized F and negligible leakage.

Figures 9a and S7 show the normalized *F* of the H1b-FQ/H2b-MB (H) and the other two H1b-FQ/H2b-MBs (M) and (L) with various concentrations of miR-21 at different assay times (30, 60, 120, 180, and 240 min) to compare the analytical performance of all localized HCR systems, respectively. The linear relationships were observed between the normalized *F* and low concentrations of miR-21 for each assay time (Figures 9b and S7). Figure 9c shows the LODs of the diffusive HCR system, semilocalized HCR system of the H1b-FQ-MB (M), and localized HCR systems of the H1b-FQ/H2b-MBs (H), (M), and (L) at different assay times (30, 60, 120, 180, and 240 min). The LODs of the H1b-FQ/H2b-MBs (H), (M), and (L) decreased with an increase in the assay time, reaching the lowest LODs after 240 min (Figure 9c); for example, LODs of the H1b-FQ/H2b-MB (H) at 30, 60, 120, 180, and 240 min were 8.9 pM, 4.9 pM, 3.6 pM, 986 fM, and 533 fM, respectively. Furthermore, LODs of H1b-FQ/H2b-MBs (H) were lower than those of the semilocalized system of the H1b-FQ-MB (M), which showed the lowest LODs among the semilocalized HCR systems. Notably, the LOD of the H1b-FQ/H2b-MB (H) at 240 min (533 fM) was ∼160 and 20 times lower than those of the diffusive HCR system (86 pM) and semilocalized HCR system of the H1b-FQ-MB (M) at 240 min (10 pM). In addition, the LOD of H1b-FQ/H2b-MB (H) at 30 min (8.9 pM) was comparable to the lowest LOD of the semilocalized HCR system of the H1b-FQ-MB (M) observed at 240 min (10 pM), allowing for an assay time that was 8 times shorter. These facts indicate that the lowest LOD and shorter assay time of the localized HCR system of H1b-FQ/H2b-MB (H) are in accordance with the above results, and thus, based on the occurrence of localized HCRs by the proximate effect with a significant increase in the local concentrations of H2b as well as H1b-FQ, the H1b-FQ/H2b-MB (H) is the most efficient scaffold for localized HCRs as well as the miRNA detection system.

Specificity is one of the most important considerations in miRNA detection; therefore, the specificity of localized HCRs using the H1b-FQ/H2b-MB (H) was evaluated with a series of miR-21s, including fully complementary miR-21, miR-21 with single-base mismatch (SM-miR-21), miR-21 with double-base mismatch (WM-miR-21), and miR-21 with triple-base mismatch (TM-miR-21) (Table S1). Figures 10 and S8a show the comparison between the normalized *F* at 240 min and the time-dependent change in the normalized *F* of H1b-FQ/H2b-MB (H) in the presence and absence (blank) of miR-21s (1 nM), respectively. The normalized *F* at 240 min (Figure 10) and the behavior of the time-dependent normalized *F* (Figure S8a) induced by WM-miR-21 and TM-miR-21 were comparable to those of the blank (miR-21 = 0 M), whereas the normalized *F* at 240 min and time-dependent normalized *F* for SM-miR-21 slightly increased because the mismatched position of SM-miR-21 was not at the complementary sequence of the toehold region of H1b-FQ.[62] Notably, miR-21 induced the highest normalized *F* at 240 min and the largest time-dependent increase in the normalized *F* compared to induction by other mismatch miR-21s, demonstrating that our miRNA detection system based on H1b-FQ/H2b-MBs (H) allows the discrimination between other mismatch miR-21s and target miR-21. Additionally, the semilocalized HCRs using the H1b-FQ-MB (M) showed similar specificity compared with the localized HCRs (Figure S8b). These facts are in accordance with the high capability of TMDRs to discriminate base mismatches.

https://doi.org/10.1021/acsami.1c09631
ACS Appl. Mater. Interfaces 2021, 13, 35533−35544

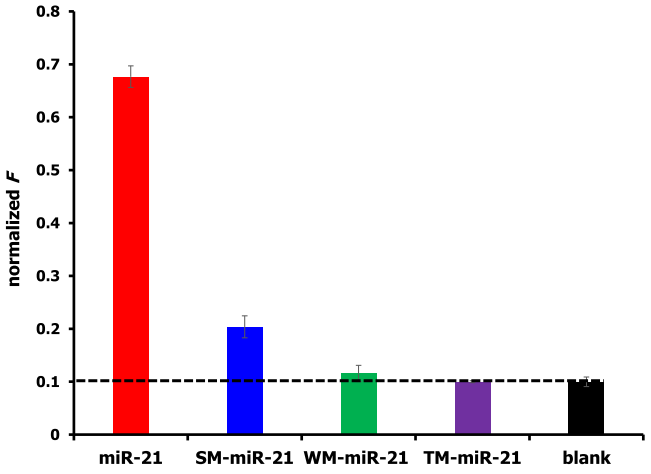

Figure 10. Normalized *F* of the localized HCR system using H1b-FQ/H2b-MB (H) for analyzing 1 nM miR-21 (target), single-base mismatch miR-21 (SM-miR-21), double-base mismatch miR-21(WM-miR-21), and triple-base mismatch miR-21 (TM-miR-21). Mean values and standard deviations were obtained from three independent experiments.

One of the most notable features of enzyme-free miRNA detection systems based on cascading TMDRs is their potential to direct detection of target miRNAs from serum samples because materials coexisting in the serum easily inhibit enzymatic reactions used for polymerase chain reaction (PCR)-based detection systems. Therefore, PCR systems require tedious and time-consuming processes, such as the isolation of total miRNAs from serum samples. Our detection system based on localized HCRs using H1b-FQ/H2b-MB (H) was applied to detect miR-21 in the presence of exosome-free fetal bovine serum (Exo-FBS) spiked with different concentrations of miR-21 (100 pM and 1 nM) as a proof of concept study. Table 1 shows the impact of Exo-FBS (10 5) on

Table 1. Detection of miR-21 in the Absence or Presence of FBS (10%) Using the H1b-FQ/H2b-MB (H) (Localized HCR System)

	FBS (−)		10% FBS (+)		
miR-21	normalized F^a	RSD (%)	normalized F^a	RSD (%)	recovery (%)
1 nM	0.677 ± 0.017	3.0	0.712 ± 0.017	2.3	95.1
100 pM	0.330 ± 0.022	6.8	0.346 ± 0.016	4.7	95.4
0 M	0.100 ± 0.009	9.1	0.102 ± 0.009	8.8	98.0

[a]Mean values and standard deviations were obtained from three independent experiments.

normalized *F* at 240 min at different concentrations of miR-21 (0 M, 100 pM, and 1 nM). Figure S9a also shows the behavior of the time-dependent normalized *F*. Notably, the normalized *F* at 240 min and the behavior of time-dependent normalized *F* of H1b-FQ/H2b-MB (H) did not change with high reproducibility even in the presence of 10% Exo-FBS. Thus, H1b-FQ/H2b-MB (H) showed a satisfactory recovery (95.1 − 98.0%) and a low relative standard deviation (RSD: 2.3−9.1%), indicating that serum does not interfere with the localized HCRs on H1b-FQ/H2b-MB (H) driven by cascading TMDRs. Similarly, the semilocalized HCR with H1b-FQ-MB (M) was able to detect miR-21 without interference from 10% FBS (Figure S9b). This indicates that the localized HCRs induced on the H1b-FQ/H2b-MB (H) scaffold have the potential for the direct detection of miRNAs from serum samples.

CONCLUSIONS

Three HCR systems were designed and constructed in this study, namely, a diffusive (conventional) HCR system, semilocalized HCR system, and localized HCR system to make quantitative comparisons of their HCR kinetics (C_t) and their analytical performance (LOD and assay time) for the enzyme-free detection of miR-21. The semilocalized HCR system was constructed using freely diffusing H2 and MBs (H1b-FQ-MBs) immobilized with one hairpin DNA (H1b-FQ) alone, and the localized HCR system was constructed using only MBs (H1b-FQ/H2b-MBs) coimmobilized with two hairpin DNAs (H1b-FQ and H2b). Additionally, MBs used for the semilocalized HCR and localized HCR systems were based on three types of nanointerface structures with different numbers of immobilized DNAs as follows: high density (H), medium density (M), and low density (L). We have shown that the DNA density on MBs significantly affects the HCR kinetics and analytical performance of the semilocalized and localized HCR systems.

In the semilocalized HCR system, the H1b-FQ-MB (H) with the largest number of immobilized H1b-FQ strands showed the slowest HCR kinetics (C_t = 90 min) because of the strong electrostatic repulsion between the dense H1-FQB strands on H1b-FQ-MBs (H) and the freely diffusing H2. Meanwhile, the H1b-FQ-MB (H) showed a higher signal-to-noise ratio than the diffusive HCR system because there was no leakage, allowing a lower LOD (21 pM within 240 min) compared to the diffusive HCR system (86 pM within 240 min). The HCR kinetics (C_t = 45 min) and the LOD (65 pM within 240 min) of the H1b-FQ-MB (L) with the smallest number of immobilized H1b-FQ strands were comparable to those of the diffusive HCR system (C_t = 45 min) because the proximate effect was limited by the long average distance between the H1b-FQ strands on the H1b-FQ-MB (L). The acceleration of HCR (C_t = 35 min) and improvement of LOD (10 pM within 240 min) were observed for the H1b-FQ-MB (M) with a medium number of immobilized H1b-FQ strands, as H1b-FQ-MB (M) with reduced electrostatic repulsion facilitated a semilocalized HCR smoothly through the proximate effect with a significant increase in the local concentrations of H1b-FQ on the MBs. This reveals that both electrostatic repulsion and the proximate effect on the MBs are important factors to consider for successful semi-localized HCR systems.

In the localized HCR system, the H1b-FQ/H2b-MB (H) with the largest number of immobilized H1b-FQ and H2b strands showed the fastest HCR kinetics (C_t = 3.6 min), the lowest LOD (533 fM within 240 min), and the shortest assay time (8.9 pM within 30 min) among the three HCR systems. The significant acceleration of the HCR kinetics is due to the occurrence of a localized HCR on the H1b-FQ/H2b-MB (H) by the proximate effect with a significant increase in the local concentrations of H2b and H1b-FQ on MBs. The HCR kinetics and LODs of H1b-FQ/H2b-MBs (M) and (L) were slower and higher with a decrease in the number of immobilized DNA strands on MBs, respectively. This is because H1b-FQ/H2b-MBs (M) and (L), with a longer average distance compared to the H1b-FQ/H2b-MB (H), are less likely to cause localized HCRs, revealing that only the

https://doi.org/10.1021/acsami.1c09631
ACS Appl. Mater. Interfaces 2021, 13, 35533−35544

proximate effect (i.e., DNA density) on MBs is an important factor for the localized HCR system. In addition, the localized HCR system using H1b-FQ/H2b-MB (H) was able to discriminate between differences in single-base mismatches and detect miR-21 even in the presence of serum. Other important issues are the size effect of MBs on the HCR kinetics and the direct detection endogenous miRNA from clinical samples, and we would like to demonstrate these issues in future work. Unlike the accelerated HCRs on 2D DNA origami scaffolds previously reported, our accelerated HCR systems do not require complex design and construction of the scaffolds, indicating that our findings open up the possibility of accelerated HCRs for practical applications.

■ ASSOCIATED CONTENT

Supporting Information

The Supporting Information is available free of charge at https://pubs.acs.org/doi/10.1021/acsami.1c09631.

Chemicals and instruments; DNA and RNA sequences (Table S1); agarose gel electrophoresis of the diffusive HCR system; preparation of H1b/miR-21-MBs (H), (M), and (L) for the determination of rate constants k_2, kinetic model for TMDRs, determination of rate constants k_1 and k_2 of TMDRs for semilocalized HCR systems; DLS measurements of the semilocalized HCR system; discrimination of base mismatches in miR-21s; and detection of miR-21 in the presence of serum (Figures S1−S9) (PDF)

■ AUTHOR INFORMATION

Corresponding Author

Motoi Oishi − *Division of Materials Science, Faculty of Pure and Applied Sciences, University of Tsukuba, Tsukuba, Ibaraki 305-8573, Japan;* orcid.org/0000-0002-1032-2164; Phone: +81-29-853-5307; Email: oishi@ims.tsukuba.ac.jp

Author

Shotaro Juji − *Division of Materials Science, Faculty of Pure and Applied Sciences, University of Tsukuba, Tsukuba, Ibaraki 305-8573, Japan*

Complete contact information is available at: https://pubs.acs.org/10.1021/acsami.1c09631

Author Contributions

The manuscript was written through the contributions of all the authors. All the authors have given approval to the final version of the manuscript.

Notes

The authors declare no competing financial interest.

■ ACKNOWLEDGMENTS

This work was in part supported by JSPS KAKENHI (Grant Number 20H02589).

■ REFERENCES

(1) Yurke, B.; Turberfield, A. J.; Mills, A. P., Jr; Simmel, F. C.; Neumann, J. L. A DNA-Fuelled Molecular Machine Made of DNA. *Nature* **2000**, *406*, 605−608.

(2) Bath, J.; Turberfield, A. J. DNA Nanomachines. *Nat. Nanotechnol.* **2007**, *2*, 275−284.

(3) Seeman, N. C. Nanomaterials Based on DNA. *Annu. Rev. Biochem.* **2010**, *79*, 65−87.

(4) Zhang, D. Y.; Seelig, G. Dynamic DNA Nanotechnology Using Strand-Displacement Reactions. *Nat. Chem.* **2011**, *3*, 103−113.

(5) Pei, H.; Zuo, X.; Zhu, D.; Huang, Q.; Fan, C. Functional DNA Nanostructures for Theranostic Applications. *Acc. Chem. Res.* **2014**, *47*, 550−559.

(6) Yang, X.; Tang, Y.; Mason, S. D.; Chen, J.; Li, F. Enzyme-Powered Three-Dimensional DNA Nanomachine for DNA Walking, Payload Release, and Biosensing. *ACS Nano* **2016**, *10*, 2324−2330.

(7) Oishi, M.; Sugiyama, S. An Efficient Particle-Based DNA Circuit System: Catalytic Disassembly of DNA/PEG-Modified Gold Nanoparticle-Magnetic Bead Composites for Colorimetric Detection of miRNA. *Small* **2016**, *12*, 5153−5158.

(8) Lv, S.; Zhang, K.; Zeng, Y.; Tang, D. Double Photosystems-Based 'Z-Scheme' Photoelectrochemical Sensing Mode for Ultrasensitive Detection of Disease Biomarker Accompanying Three-Dimensional DNA Walker. *Anal. Chem.* **2018**, *90*, 7086−7093.

(9) Yang, K.; Wang, H.; Ma, N.; Zeng, M.; Luo, H.; He, D. Programmable Target-Initiated DNAzyme Walker Walking along a Spatially Isolated and Highly Hybridizable Substrate Track on a Nanoparticle Surface. *ACS Appl. Mater. Interfaces* **2018**, *10*, 44546−44553.

(10) Oishi, M. Comparative Study of DNA Circuit System-Based Proportional and Exponential Amplification Strategies for Enzyme-Free and Rapid Detection of miRNA at Room Temperature. *ACS Omega* **2018**, *3*, 3321−3329.

(11) He, X.; Zeng, T.; Li, Z.; Wang, G.; Ma, N. Catalytic Molecular Imaging of MicroRNA in Living Cells by DNA-Programmed Nanoparticle Disassembly. *Angew. Chem., Int. Ed.* **2016**, *55*, 3073−3076.

(12) Liang, C.-P.; Ma, P.-Q.; Liu, H.; Guo, X.; Yin, B.-C.; Ye, B.-C. Rational Engineering of a Dynamic, Entropy-Driven DNA Nanomachine for Intracellular MicroRNA Imaging. *Angew. Chem., Int. Ed.* **2017**, *56*, 9077−9081.

(13) Xiao, M.; Wang, X.; Li, L.; Pei, H. Stochastic RNA Walkers for Intracellular MicroRNA Imaging. *Anal. Chem.* **2019**, *91*, 11253−11258.

(14) Xu, X.; Zhang, P.; Zhang, R.; Zhang, N.; Jiang, W. A DNA Walker Powered by Endogenous Enzymes for Imaging Uracil-DNA Glycosylase Activity in Living Cells. *Chem. Commun.* **2019**, *55*, 6026−6029.

(15) Douglas, S. M.; Bachelet, I.; Church, G. M. A Logic-Gated Nanorobot for Targeted Transport of Molecular Payloads. *Science* **2012**, *335*, 831−834.

(16) Zhu, D.; Pei, H.; Yao, G.; Wang, L.; Su, S.; Chao, J.; Wang, L.; Aldalbahi, A.; Song, S.; Shi, J.; Hu, J.; Fan, C.; Zuo, X. A Surface-Confined Proton-Driven DNA Pump Using a Dynamic 3D DNA Scaffold. *Adv. Mater.* **2016**, *28*, 6860−6865.

(17) Cangialosi, A.; Yoon, C.; Liu, J.; Huang, Q.; Guo, J.; Nguyen, T. D.; Gracias, D. H.; Schulman, R. DNA Sequence-Directed Shape Change of Photopatterned Hydrogels via High-Degree Swelling. *Science* **2017**, *357*, 1126−1130.

(18) Oishi, M.; Nakatani, K. Dynamically Programmed Switchable DNA Hydrogels Based on a DNA Circuit Mechanism. *Small* **2019**, *15*, No. 1900490.

(19) Zhao, Z.; Wang, C.; Yan, H.; Liu, Y. Soft Robotics Programmed with Double Crosslinking DNA Hydrogels. *Adv. Funct. Mater.* **2019**, *29*, No. 1905911.

(20) Oishi, M.; Saito, K. Simple Single-Legged DNA Walkers at Diffusion-Limited Nanointerfaces of Gold Nanoparticles Driven by a DNA Circuit Mechanism. *ACS Nano* **2020**, *14*, 3477−3489.

(21) Qian, L.; Winfree, E.; Bruck, J. Neural Network Computation with DNA Strand Displacement Cascades. *Nature* **2011**, *475*, 368−372.

(22) Chen, Y.-J.; Dalchau, N.; Srinivas, N.; Phillips, A.; Cardelli, L.; Soloveichik, D.; Seelig, G. Programmable Chemical Controllers Made from DNA. *Nat. Nanotechnol.* **2013**, *8*, 755−762.

(23) Groves, B.; Chen, Y.-J.; Zurla, C.; Pochekailov, S.; Kirschman, J. L.; Santangelo, P. J.; Seelig, G. Computing in Mammalian Cells with Nucleic Acid Strand Exchange. *Nat. Nanotechnol.* **2016**, *11*, 287−294.
(24) Boemo, M. A.; Lucas, A. E.; Turberfield, A. J.; Cardelli, L. The Formal Language and Design Principles of Autonomous DNA Walker Circuits. *ACS Synth. Biol.* **2016**, *5*, 878−884.
(25) Yurke, B.; Mills, A. P., Jr. Using DNA to Power Nanostructures. *Genet. Progr. Evol. Mach.* **2003**, *4*, 111−122.
(26) Green, S. J.; Lubrich, D.; Turberfield, A. J. DNA Hairpins: Fuel for Autonomous DNA Devices. *Biophys. J.* **2006**, *91*, 2966−2975.
(27) Zhang, D. Y.; Winfree, E. Control of DNA Strand Displacement Kinetics Using Toehold Exchange. *J. Am. Chem. Soc.* **2009**, *131*, 17303−17314.
(28) Srinivas, N.; Ouldridge, T. E.; Sulc, P.; Schaeffer, J. M.; Yurke, B.; Louis, A. A.; Doye, J. P. K.; Winfree, E. On the Biophysics and Kinetics of Toehold-Mediated DNA Strand Displacement. *Nucleic Acids Res.* **2013**, *41*, 10641−10658.
(29) Dirks, R. M.; Pierce, N. A. Triggered Amplification by Hybridization Chain Reaction. *Proc. Natl. Acad. Sci. U.S.A.* **2004**, *101*, 15275−15278.
(30) Venkataraman, S.; Dirks, R. M.; Rothemund, P. W. K.; Winfree, E.; Pierce, N. A. An Autonomous Polymerization Motor Powered by DNA Hybridization. *Nat. Nanotechnol.* **2007**, *2*, 490−494.
(31) Lubrich, D.; Green, S. J.; Turberfield, A. J. Kinetically Controlled Self-Assembly of DNA Oligomers. *J. Am. Chem. Soc.* **2009**, *131*, 2422−2423.
(32) Choi, H. M. T.; Chang, J. Y.; Trinh, L. A.; Padilla, J. E.; Fraser, S. E.; Pierce, N. A. Programmable in Situ Amplification for Multiplexed Imaging of mRNA Expression. *Nat. Biotechnol.* **2010**, *28*, 1208−1212.
(33) Yin, P.; Choi, H. M. T.; Calvert, C. R.; Pierce, N. A. Programming Biomolecular Self-Assembly Pathways. *Nature* **2008**, *451*, 318−322.
(34) Li, B.; Ellington, A. D.; Chen, X. Rational, Modular Adaptation of Enzyme-Free DNA Circuits to Multiple Detection Methods. *Nucleic Acids Res.* **2011**, *39*, No. e110.
(35) Zhang, D. Y.; Turberfield, A. J.; Yurke, B.; Winfree, E. Engineering Entropy-Driven Reactions and Networks Catalyzed by DNA. *Science* **2007**, *318*, 1121−1125.
(36) Jiang, Y. S.; Li, B.; Milligan, J. N.; Bhadra, S.; Ellington, A. D. Real-time Detection of Isothermal Amplification Reactions with Thermostable Catalytic Hairpin Assembly. *J. Am. Chem. Soc.* **2013**, *135*, 7430−7433.
(37) Jiang, Y. S.; Bhadra, S.; Li, B.; Ellington, A. D. Mismatches Improve the Performance of Strand-Displacement Nucleic Acid Circuits. *Angew. Chem., Int. Ed.* **2014**, *53*, 1845−1848.
(38) Dalchau, N.; Chandran, H.; Gopalkrishnan, N.; Phillips, A.; Reif, J. Probabilistic Analysis of Localized DNA Hybridization Circuits. *ACS Synth. Biol.* **2015**, *4*, 898−913.
(39) Wu, Z.; Liu, G.-Q.; Yang, X.-L.; Jiang, J-H. Electrostatic Nucleic Acid Nanoassembly Enables Hybridization Chain Reaction in Living Cells for Ultrasensitive mRNA Imaging. *J. Am. Chem. Soc.* **2015**, *137*, 6829−6836.
(40) Li, L.; Feng, J.; Liu, H.; Li, Q.; Tong, L.; Tang, B. Two-Color Imaging of MicroRNA with Enzyme-Free Signal Amplification via Hybridization Chain Reactions in Living Cells. *Chem. Sci.* **2016**, *7*, 1940−1945.
(41) Leino, M.; Heldin, J.; Sander, M. R.; Kermpatsou, D.; Raykova, D.; Koos, B.; Söderberg, O. Optimization of Proximity-Dependent Initiation of Hybridization Chain Reaction for Improved Performance. *Mol. Syst. Des. Eng.* **2019**, *4*, 1058−1065.
(42) Engelen, W.; Wijnands, S. P. W.; Merkx, M. Accelerating DNA-Based Computing on a Supramolecular Polymer. *J. Am. Chem. Soc.* **2018**, *140*, 9758−9767.
(43) Bui, H.; Miao, V.; Garg, S.; Mokhtar, R.; Song, T.; Reif, J. Design and Analysis of Localized DNA Hybridization Chain Reactions. *Small* **2017**, *13*, No. 1602983.
(44) Ren, K.; Xu, Y.; Liu, Y.; Yang, M.; Ju, H. A Responsive "Nano String Light" for Highly Efficient mRNA Imaging in Living Cells via Accelerated DNA Cascade Reaction. *ACS Nano* **2018**, *12*, 263−271.
(45) Helmig, S.; Gothelf, K. V. AFM Imaging of Hybridization Chain Reaction Mediated Signal Transmission between Two DNA Origami Structures. *Angew. Chem., Int. Ed.* **2017**, *56*, 13633−13636.
(46) Chatterjee, G.; Dalchau, N.; Muscat, R. A.; Phillips, A.; Seelig, G. A Spatially Localized Architecture for Fast and Modular DNA Computing. *Nat. Nanotechnol.* **2017**, *12*, 920−927.
(47) Bui, H.; Shah, S.; Mokhtar, R.; Song, T.; Garg, S.; Reif, J. Localized DNA Hybridization Chain Reactions on DNA Origami. *ACS Nano* **2018**, *12*, 1146−1155.
(48) Oishi, M. Enzyme-Free and Isothermal Detection of Micro-RNA Based on Click-Chemical Ligation-Assisted Hybridization Coupled with Hybridization Chain Reaction Signal Amplification. *Anal. Bioanal. Chem.* **2015**, *407*, 4165−4172.
(49) Kato, D.; Oishi, M. Ultrasensitive Detection of DNA and RNA Based on Enzyme-Free Click Chemical Ligation Chain Reaction on Dispersed Gold Nanoparticles. *ACS Nano* **2014**, *8*, 9988−9997.
(50) Valentini, P.; Fiammengo, R.; Sabella, S.; Gariboldi, M.; Maiorano, G.; Cingolani, R.; Pompa, P. P. Gold-Nanoparticle-Based Colorimetric Discrimination of Cancer-Related Point Mutations with Picomolar Sensitivity. *ACS Nano* **2013**, *7*, 5530−5538.
(51) Li, J.; Song, S.; Liu, X.; Wang, L.; Pan, D.; Huang, Q.; Zhao, Y.; Fan, C. Enzyme-Based Multi-Component Optical Nanoprobes for Sequence-Specific Detection of DNA Hybridization. *Adv. Mater.* **2008**, *20*, 497−500.
(52) Yin, B.-C.; Liu, Y.-Q.; Ye, B.-C. One-step, Multiplexed Fluorescence Detection of MicroRNAs Based on Duplex-Specific Nuclease Signal Amplification. *J. Am. Chem. Soc.* **2012**, *134*, 5064−5067.
(53) Miao, X.; Cheng, Z.; Ma, H.; Li, Z.; Xue, N.; Wang, P. Label-Free Platform for MicroRNA Detection Based on the Fluorescence Quenching of Positively Charged Gold Nanoparticles to Silver Nanoclusters. *Anal. Chem.* **2018**, *90*, 1098−1103.
(54) Yang, C.; Wang, H.; Tang, H.; Zhao, D.; Li, Y. A Simple Strategy for the Fabrication of Gold-Modified Single Nanopores and Its Application for miRNA Sensing. *Chem. Commun.* **2019**, *55*, 10288−10291.
(55) Harris, D. C. Applications of Spectrophotometer. In *Quantitative Chemical Analysis*, 8th ed.; W. H. Freeman and Co.: New York, 2010; pp 419−444.
(56) Zhao, Y.; Chen, F.; Li, Q.; Wang, L.; Fan, C. Isothermal Amplification of Nucleic Acids. *Chem. Rev.* **2015**, *115*, 12491−12545.
(57) Yao, D.; Wang, B.; Xiao, S.; Song, T.; Huang, F.; Liang, H. What Controls the "Off/On Switch" in the Toehold-Mediated Strand Displacement Reaction on DNA Conjugated Gold Nanoparticles? *Langmuir* **2015**, *31*, 7055−7061.
(58) Takashima, A.; Oishi, M. Kinetic Study of DNA Hybridization on DNA-Modified Gold Nanoparticles with Engineered Nano-Interfaces. *RSC Adv.* **2015**, *5*, 76014−76018.
(59) Lam, M. K.; Gadzikwa, T.; Nguyen, T.; Kausar, A.; Alladin-Mustan, B. S.; Sikder, M. D.; Gibbs-Davis, J. M. Tuning Toehold Length and Temperature to Achieve Rapid, Colorimetric Detection of DNA from the Disassembly of DNA-Gold Nanoparticle Aggregates. *Langmuir* **2016**, *32*, 1585−1590.
(60) Li, M.-X.; Xu, C.-H.; Zhang, N.; Qian, G.-S.; Zhao, W.; Xu, J.-J.; Chen, H.-Y. Exploration of the Kinetics of Toehold-Mediated Strand Displacement via Plasmon Rulers. *ACS Nano* **2018**, *12*, 3341−3350.
(61) Hill, H. D.; Millstone, J. E.; Banholzer, M. J.; Mirkin, C. A. The Role Radius of Curvature Plays in Thiolated Oligonucleotide Loading on Gold Nanoparticles. *ACS Nano* **2009**, *3*, 418−424.
(62) Chen, S. X.; Seelig, G. An Engineered Kinetic Amplification Mechanism for Single Nucleotide Variant Discrimination by DNA Hybridization Probes. *J. Am. Chem. Soc.* **2016**, *138*, 5076−5086.

https://doi.org/10.1021/acsami.1c09631
ACS Appl. Mater. Interfaces 2021, 13, 35533−35544